PHYSICAL REVIEW B **92**, 235104 (2015)

Fermi surface interconnectivity and topology in Weyl fermion semimetals TaAs, TaP, NbAs, and NbP

Chi-Cheng Lee,[1,2] Su-Yang Xu,[3] Shin-Ming Huang,[1,2] Daniel S. Sanchez,[3] Ilya Belopolski,[3] Guoqing Chang,[1,2]
Guang Bian,[3] Nasser Alidoust,[3] Hao Zheng,[3] Madhab Neupane,[3,4] Baokai Wang,[1,2,5] Arun Bansil,[5]
M. Zahid Hasan,[3,6,*] and Hsin Lin[1,2,†]
[1]*Centre for Advanced 2D Materials and Graphene Research Centre, National University of Singapore, 6 Science Drive 2, Singapore 117546*
[2]*Department of Physics, National University of Singapore, 2 Science Drive 3, Singapore 117542*
[3]*Laboratory for Topological Quantum Matter and Spectroscopy (B7), Department of Physics, Princeton University, Princeton, New Jersey 08544, USA*
[4]*Condensed Matter and Magnet Science Group, Los Alamos National Laboratory, Los Alamos, New Mexico 87545, USA*
[5]*Department of Physics, Northeastern University, Boston, Massachusetts 02115, USA*
[6]*Princeton Center for Complex Materials, Princeton Institute for the Science and Technology of Materials, Princeton University, Princeton, New Jersey 08544, USA*

(Received 27 August 2015; revised manuscript received 3 October 2015; published 1 December 2015)

The family of binary compounds including TaAs, TaP, NbAs, and NbP was recently discovered as the first realization of Weyl semimetals. In order to develop a comprehensive description of the charge carriers in these Weyl semimetals, we performed detailed and systematic electronic band structure calculations which reveal the nature of Fermi surfaces and their complex interconnectivity in TaAs, TaP, NbAs, and NbP. Our work reports a comparative and comprehensive study of Fermi surface topology and band structure details of all known members of the Weyl semimetal family and hence provides the fundamental knowledge for realizing the many predicted exotic topological quantum physics of Weyl semimetals based on the TaAs class of materials.

DOI: 10.1103/PhysRevB.92.235104 PACS number(s): 71.18.+y, 71.20.−b, 73.20.At

I. INTRODUCTION

The discovery of Dirac fermions as low-energy quasiparticle excitations in graphene and on the surfaces of topological insulators has drawn significant attention in both fundamental physics research and device applications [1–34]. Since these Dirac-like fermions propagate as massless relativistic particles, they behave differently from the conventional charge carriers in metals, semiconductors, and insulators. Recently, a new form of massless fermions with lifted degeneracy at the nodal point, from fourfold to two-fold, has been proposed to exist in condensed-matter systems through a time-reversal- or inversion-symmetry-breaking mechanism. This symmetry-breaking operation modifies the quasiparticle's dispersion relation from a Dirac to a Weyl equation [1–34]. Many theoretical proposals exist for realizing Weyl semimetals that possess interesting physical properties, such as discontinuous Fermi arcs and negative magnetoresistance due to the chiral anomaly [4,6–10,19–29,31,32,34]. A Weyl node with definite chirality is associated with the Berry curvature and may be thought of as realizations of magnetic monopoles in momentum space [30,35].

Recent theoretical works have proposed the realization of the Weyl semimetal state in the inversion-symmetry-breaking TaAs family [11,13]. Shortly after the prediction, the first Weyl semimetal was experimentally discovered in TaAs [12]. The electronic Weyl semimetal state in TaAs was experimentally observed through photoemission spectroscopy [12,14]. Electrical transport experiments have shown that TaAs has very high mobility [36] and therefore is consistent with the protected nature of the Weyl fermions and reported signatures of the chiral anomaly [37,38]. Soon after the initial experimental discovery, other independent photoemission experimental works confirmed the Weyl semimetal state in TaAs and, furthermore, the Weyl state in other members of the same family, which includes NbAs and TaP [39–43]. This discovery paves the way for realizing the many predicted exotic topological quantum phenomena of Weyl semimetals in the TaAs class of materials [9,25–34]. For any ongoing [36–38,43–52] or future experiments on these materials, systematic knowledge of the band structure and Fermi surface is crucial and fundamental in understanding and interpreting their data and observations. However, surprisingly, a comprehensive study of the band structure details of the TaAs Weyl semimetal family has been lacking. Here, we report the first comparative and comprehensive study of Fermi surface topology and band structure details of all known members of the Weyl semimetal family.

Previous theoretical studies of this family focused on establishing TaAs as a Weyl semimetal and therefore reported only a few key aspects of the electronic structure for that purpose. On the other hand, many systematic details of the band structure, which are crucial for spectroscopy and transport studies, have not been studied. Here, we report a comparative and comprehensive study of Fermi surface topology and band structure details of all known members of the Weyl semimetal family. Our work is crucial and fundamental for future investigations of the topological Weyl semimetal phase from theoretical, experimental, and application perspectives based on the TaAs class of materials.

This paper is organized in the following manner: In Sec. II we provide the computational details. In Sec. III, electronic band structures and densities of states are studied to improve our basic understanding of these four compounds. In Sec.

---

[*] Corresponding author: mzhasan@princeton.edu

[†] Corresponding author: nilnish@gmail.com

TABLE I. Experimental lattice parameters (see Fig. 1).

	TaAs	TaP	NbAs	NbP
a (Å)	3.437	3.318	3.452	3.334
c (Å)	11.656	11.363	11.679	11.376
u/c	0.333	0.334	0.333	0.334

IV, we discuss the details of the Fermi velocities of Weyl fermions and Fermi surfaces. Finally, in Sec. V we present a brief discussion covering the important conclusions reached.

II. COMPUTATIONAL DETAILS

First-principles calculations of TaAs, TaP, NbAs, and NbP, which have space group $I4_1md$ (109), a body-centered-tetragonal structure, were performed using the OPENMX code. The OPENMX code was based on norm-conserving pseudopotentials generated with multiple reference energies [53] and optimized pseudoatomic basis functions [54,55]. For each Ta atom, three, two, two, and one optimized radial functions were allocated for the s-, p-, d-, and f orbitals ($s3p2d2f1$), respectively. For As, Nb, and P atoms, $s3p3d3f2$, $s3p3d3f1$, and $s3p3d2f1$ were adopted, respectively. A cutoff radius of 7 bohrs was adopted for Ta, Nb, and P basis functions, while a 9-bohr cutoff radius was used for the As basis functions. The spin-orbit coupling was taken into account through j-dependent pseudopotentials [56], and the generalized gradient approximation (GGA) was adopted for the exchange-correlation energy functional [57–60]. A cutoff energy of 1000 Ry was used for numerical integrations and for the solution of the Poisson equation. For the quality of k-point sampling, a $17 \times 17 \times 5$ mesh for the conventional unit cell was adopted. The experimental lattice parameters were chosen in the calculations and are listed in Table I. The conventional unit cell and first Brillouin zone of the primitive unit cell of the representative TaAs is plotted in Fig. 1.

Throughout this paper, for brevity, we will label the crystal momentum in units of $(2\pi/a, 2\pi/a, 2\pi/c)$ unless otherwise specified.

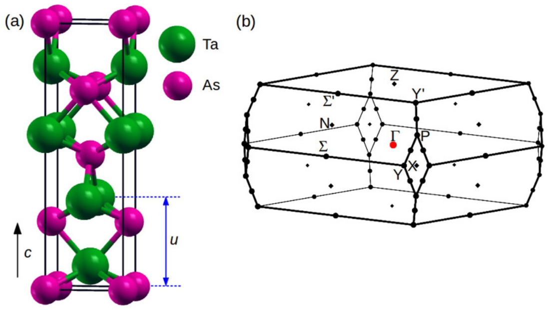

FIG. 1. (Color online) (a) Conventional unit cell of TaAs. (b) Primitive first Brillouin zone of TaAs. TaP, NbAs, and NbP share the same body-centered-tetragonal structure with different lattice parameters, which are listed in Table I.

III. ELECTRONIC STRUCTURE

In this section, the electronic band structure and density of states for the four Weyl semimetal compounds are presented. With the combination of Ta or Nb and As or P, very similar electronic structures can be found and therefore illustrate flexibility in realizing Weyl fermions among these four elements.

A. Symmetry

The relevant symmetry elements in the TaAs family (space group $I4_1md$) is the fourfold screw rotations along the z axis and two mirror reflections with respect to the x and y axes. Due to the lack of inversion symmetry, the rotation axis cannot sit perpendicular to the mirror planes. The combination of screw rotations and mirror reflections results in diagonal glide planes. Because the screw rotation and glide reflection are compound symmetry operations of translation and point-group operations, for a specific surface termination the surface states will not contain these compound symmetries. For the bulk, however, due to translation symmetry, the energy spectrum displays the C_4 and mirror symmetries. In k space, there are mirror planes at $k_x = 0$, $k_y = 0$, and $k_x \pm k_y = 0$. The $k_x = 0$ and $k_y = 0$ mirror planes are important for the realization of Weyl nodes. On the mirror plane, each band can possess a mirror eigenvalue of either $+1$ or -1 ($+i$ or $-i$) in the absence (presence) of spin-orbit coupling. Bands with opposite mirror eigenvalues are allowed to cross, and those with the same mirror eigenvalues are permitted only to anticross. The other symmetry is time reversal, which is not a spatial symmetry. Since time-reversal symmetry relates $\vec{k}$ and $-\vec{k}$ states, its combination with the twofold rotation results in the energy spectrum being symmetric with respect to the $k_z = 0,1$ planes.

Since a Weyl node is characterized by a chirality of ± 1, which is defined by the integration of Berry curvature, a pseudovector, over a closed k-space surface (in units of 2π) [30,35], Weyl nodes related by mirror symmetry will possess opposite chirality, while those related by rotation and time-reversal symmetries will have the same chirality. Thus, a mirror pair of Weyl nodes, as mirror images, will possess, relative to each other, opposite chirality, and two Weyl nodes at equal k_x and k_y but opposite k_z will have the same chirality. Furthermore, the closed surface can be extended to a Fermi surface, yielding a Chern number for the Fermi surface [61] and therefore reflecting the net chirality of the enclosed Weyl nodes.

B. Band structure

The electronic band structures of TaAs, TaP, NbAs, and NbP with and without spin-orbit coupling are shown in Figs. 2, 3, 4, and 5, respectively. As expected, the band structures of these four Weyl semimetal compounds are characterized by the d orbitals of the Ta or Nb atom, and the p orbitals of the As or P atom are similar to one another near the Fermi energy. In the absence of spin-orbit coupling, the valence and conduction bands cross and form closed rings that are bounded on the mirror planes ($k_x = 0$ and $k_y = 0$ planes) due to the fact that both bands have opposite mirror eigenvalues. For the four Weyl semimetal compounds the nodal rings on the $k_x = 0$ mirror planes are shown in Fig. 6. Similarly, the location of nodal

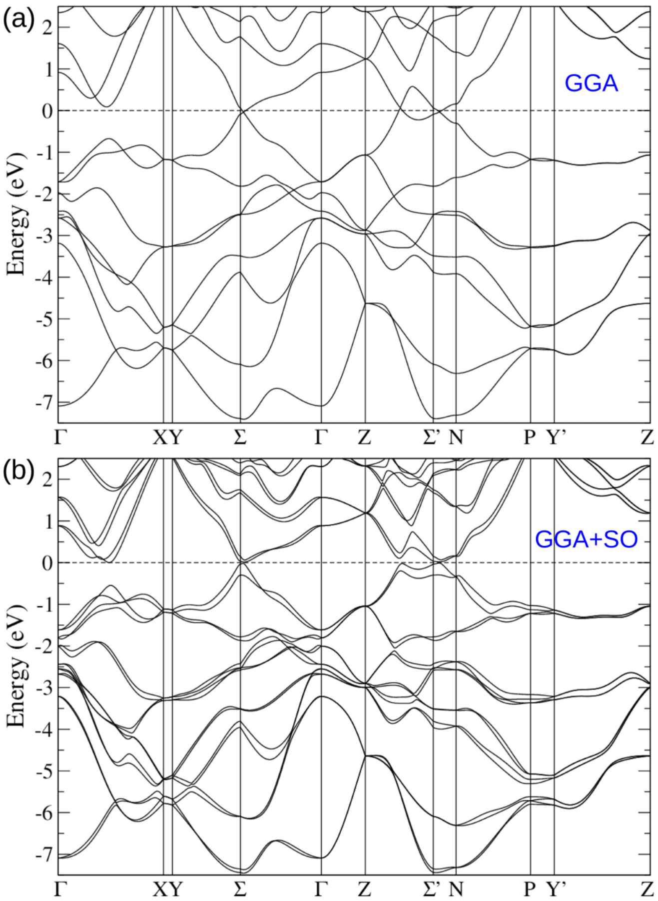

FIG. 2. (Color online) Electronic band structure of TaAs (a) without and (b) with spin-orbit coupling.

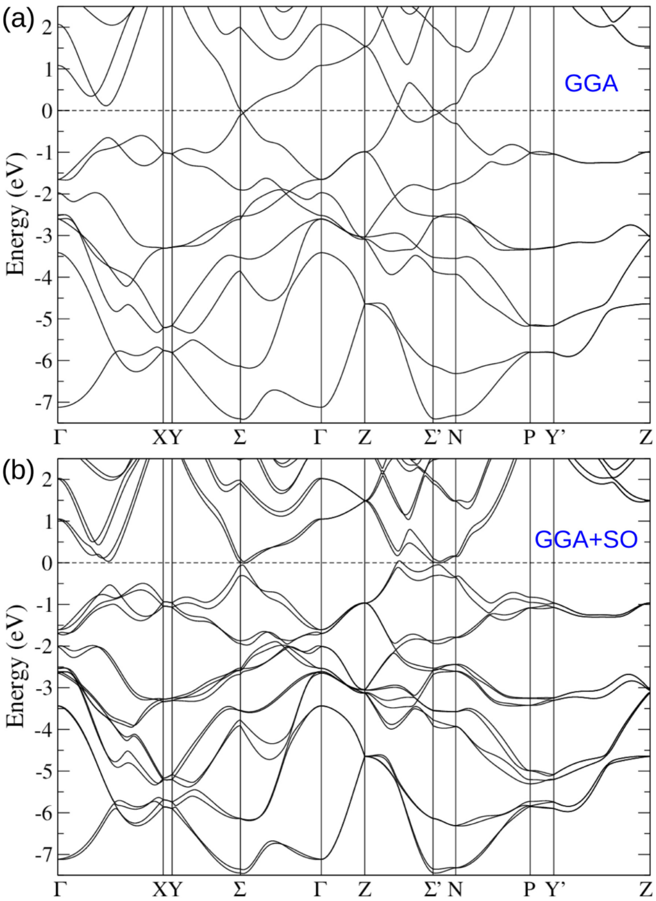

FIG. 3. (Color online) Electronic band structure of TaP (a) without and (b) with spin-orbit coupling.

rings on the $k_y = 0$ mirror planes can be found by applying a C_4 rotation. Again, note that away from the mirror planes, which lack the necessary symmetry requirements, accidental band crossings are not found.

In the presence of spin-orbit coupling, the aforementioned nodal rings no longer exist. The valence and conduction bands become fully gapped along the high-symmetry lines, as shown in Figs. 2, 3, 4, and 5. The gap opening is smaller when replacing the Ta atom with an Nb atom, which indicates weaker spin-orbit coupling in NbAs and NbP and is consistent with the strong spin-orbit coupling in heavy elements.

The disappearance of nodal rings is followed by the appearance of Weyl nodes. Pairs of Weyl nodes around the rings with opposite chirality on the two sides of the mirror planes are found [11,13]. For each ring in Fig. 6, three pairs of Weyl nodes are generated, and their locations, projected on the $k_x = 0$ plane, are indicated by the solid circles. The location of the other pairs of Weyl nodes can be obtained by applying a C_4 rotation, which uncovers 24 Weyl nodes for the first Brillouin zone. The detailed k-space coordinates and energies of two representative Weyl nodes are given in Table II. We denote Weyl nodes by W_1 for those at $k_z = n$ (multiples of $\frac{2\pi}{c}$) and by W_2 otherwise. The energies of W_1 are lower than those of W_2 for all of the studied compounds. For a Weyl node below (above) the Fermi energy, an electronlike (holelike) Fermi surface will enclose a Weyl node.

Although the nodal rings are destroyed by spin-orbit coupling, new nodal rings are allowed to be created since the closest valence and conduction bands possess opposite mirror eigenvalues, $\pm i$. In other words, bands can cross on the plane with suitable hopping parameters. In NbAs, such a ring is found at $\vec{k} \approx (0,0.41,1.47)$ with a tiny radius <0.005. The negligible k-space area is in accordance with the energy overlap of only $\leqslant 0.2$ meV for the ring. The energy of the ring is located approximately 5.4 meV above the Fermi energy. Since the energy overlap is tiny and occurs above the Fermi energy, we neglect the significance of this overlap in this study. The fact that spin-orbit coupling can annihilate or keep the nodal lines indicates that these lines depend on the presence of mirror symmetry but are not protected by it. However, parity of the number of nodal lines is conserved because of topology.

C. Density of states

TaAs, TaP, NbAs, and NbP have similar electron configurations in the outer shells, namely, d^3s^2 for Ta and Nb and p^3 for As and P. In order to fill the outermost p orbitals of As and P, As^{3-}, P^{3-}, Ta^{3+}, and Nb^{3+} are expected according to the ionic-bonding picture, which should leave the Ta d or Nb d orbitals with a higher energy than the fully filled As p or P p orbitals. In Fig. 7, the partial densities of states for Ta d, Nb d, As p, and P p are presented. One can directly observe that the

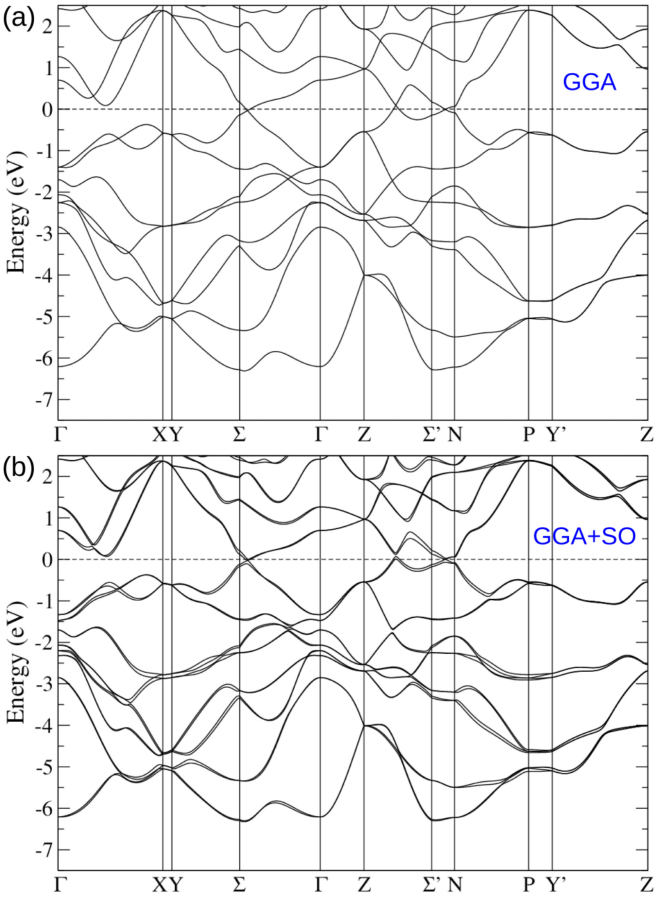

FIG. 4. (Color online) Electronic band structure of NbAs (a) without and (b) with spin-orbit coupling.

d orbitals are strongly hybridized with the p orbitals. Although p character leads to the major contributions in the bottom band, the p orbitals are not fully occupied. In fact, the occupation numbers obtained in the basis of linear combination of atomic orbitals give only approximately half-filled p orbitals, and the p orbitals also contribute to the energy above the Fermi energy. Therefore, it is inadequate to neglect the effect of p orbitals near the Fermi energy.

A simple picture to understand the obtained density of states is that of the Ta or Nb d orbitals hopping strongly to the As or P p orbitals and giving rise to the bonding and antibonding bands across the Fermi energy. The Ta or Nb s orbital also participates in the hybridization and does not donate itself completely. With this hybridization scheme, the semimetal feature is formed, which shows the valence and conduction bands separated by a valley-shaped density of states at the Fermi energy. The density of states is not zero at the Fermi energy due to the lack of particle-hole symmetry and the two distinct Weyl nodes (W_1, W_2) possessing different energies for each compound. Furthermore, the valence and conduction bands are found to cut through the Fermi energy and therefore form hole and electron pockets, respectively. Note that the major contribution to the density of states around the Fermi energy is of d character. The bonding and antibonding p orbitals are split into much lower and higher energy.

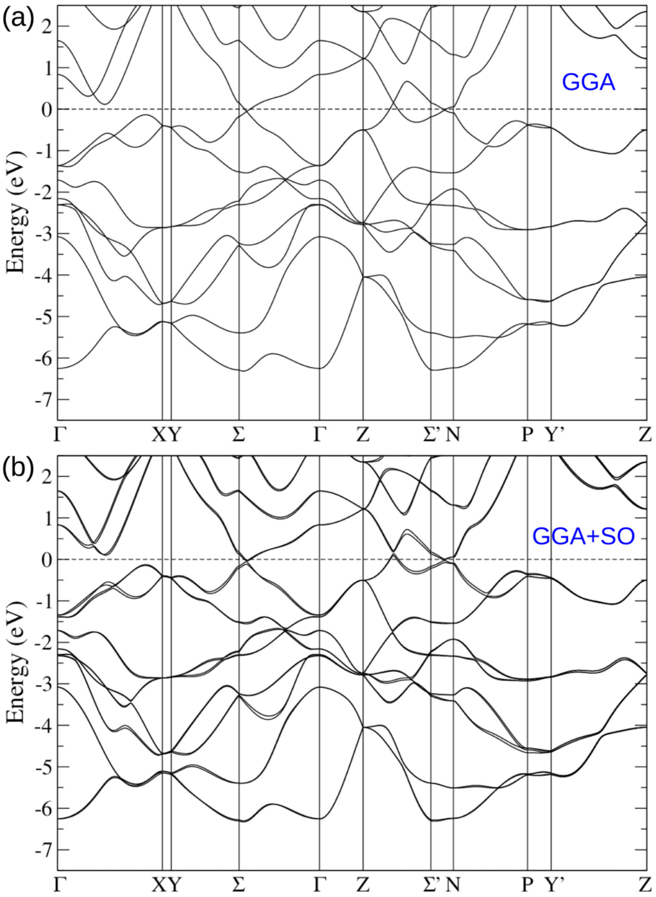

FIG. 5. (Color online) Electronic band structure of NbP (a) without and (b) with spin-orbit coupling.

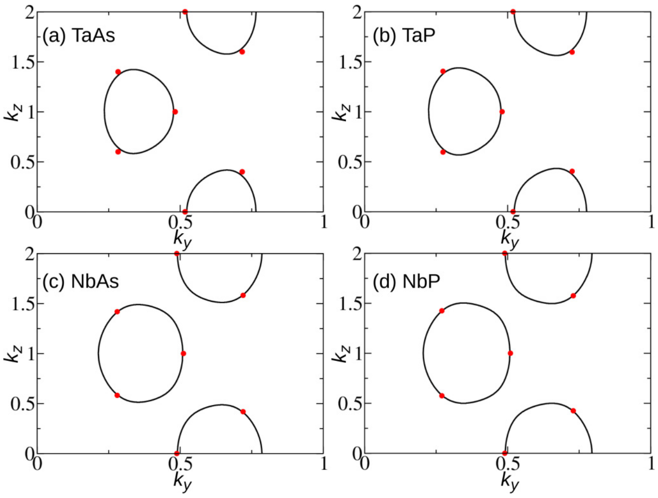

FIG. 6. (Color online) Line nodes on the $k_x = 0$ plane formed by the crossing of valence and conduction bands in (a) TaAs, (b) TaP, (c) NbAs, and (d) NbP without spin-orbit coupling. The red solid circles indicated the projection of Weyl nodes on the $k_x = 0$ plane after turning on the spin-orbit coupling. For each circle, two Weyl nodes of opposite chiralities on two sides of the $k_x = 0$ plane are found.

Some additional information can be obtained from Fig. 7. TaAs and TaP share a wider bandwidth relative to the

TABLE II. The coordinates (in units of reciprocal lattice vectors of the conventional unit cell) and energies (in eV) of two representative distinct Weyl nodes denoted W_1 and W_2. In each compound the energy of W_2 is higher than that of W_1. Here, ± stands for a mirror pair of Weyl nodes.

	Coordinate of W_1	Energy of W_1
TaAs	(±0.0072, 0.4827, 1.0000)	−0.0221
TaP	(±0.0074, 0.4809, 1.0000)	−0.0531
NbAs	(±0.0025, 0.5116, 1.0000)	−0.0322
NbP	(±0.0028, 0.5099, 1.0000)	−0.0534
	Coordinate of W_2	Energy of W_2
TaAs	(±0.0185, 0.2831, 0.6000)	−0.0089
TaP	(±0.0156, 0.2743, 0.5958)	0.0196
NbAs	(±0.0062, 0.2800, 0.5816)	0.0042
NbP	(±0.0049, 0.2703, 0.5750)	0.0259

narrower bandwidth of NbAs and NbP, which reflects that $5d$ electrons are more delocalized than $4d$ electrons and that the replacement of As p by P p has less of an effect on the overall density of states. However, it is clearly observed that the density of states of P p in TaP is slightly lower than that of As p in TaAs. In addition, the density of states of P p in NbP is lower than that of As p in NbAs. This indicates that P p orbitals lose more electrons and are farther away from the picture of fully filled p orbitals. Another observation is that Nb d orbitals in NbP show the largest area below the Fermi energy and therefore possess the most d electrons out of the family of four Weyl semimetal compounds.

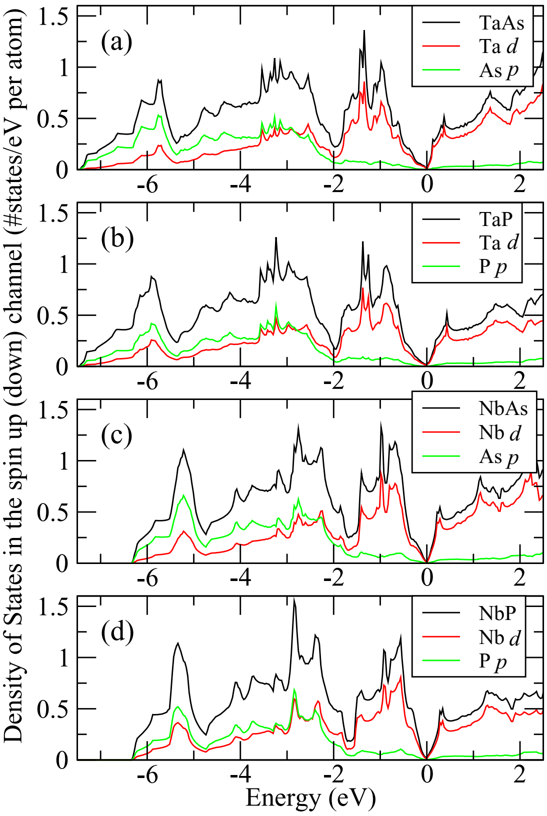

FIG. 7. (Color online) The orbital contributions of Ta d or Nb d and As p or P p in the density of states with spin-orbit coupling for (a) TaAs, (b) TaP, (c) NbAs, and (d) NbP. The d and p contributions are colored red and green, respectively. The total formula contributions are plotted by black lines.

IV. CHARGE CARRIERS

In this section we investigate the properties of the Fermi surface. We first show the Fermi velocities of the Weyl fermions and the band dispersion between the energies of Weyl nodes and the Fermi energy for W_1 and W_2. Because of symmetry, we will show results for W_1 and W_2 at positive k_x, listed in Table II. Then the detailed studies of all the electron- and holelike Fermi surfaces found in the four Weyl semimetal compounds are discussed.

A. Fermi velocity of Weyl fermion

In Weyl semimetals, the energies of Weyl nodes are close to the Fermi energy. Therefore, the physical properties of Weyl fermions are easy to experimentally access by slightly electron or hole doping the systems. The velocity of an electron can be calculated by $(1/\hbar)dE/dk$. The details of how the slope of the band dispersion varies between W_1 or W_2 and the Fermi energy can be found in Figs. 8 and 9, respectively. The velocities at

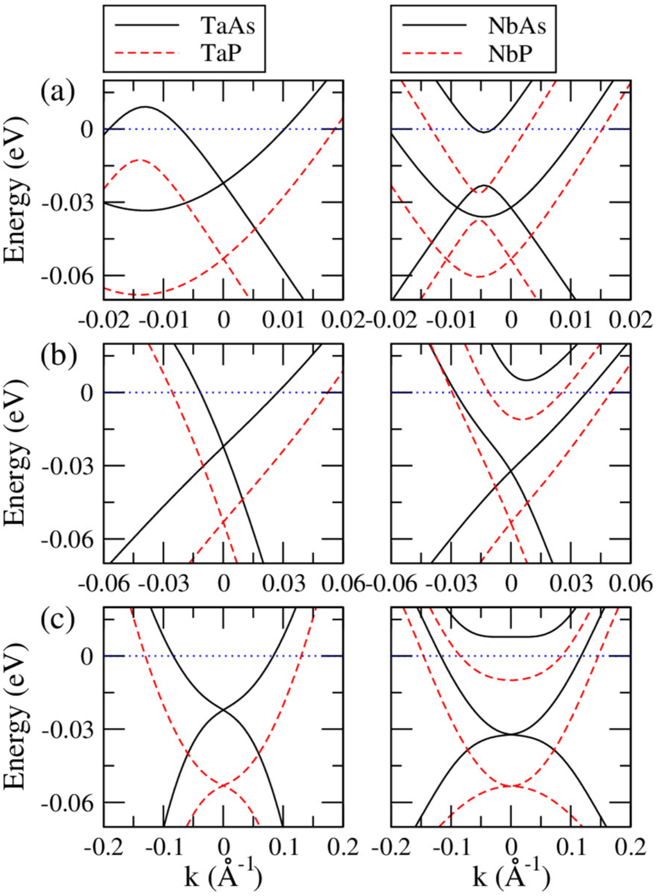

FIG. 8. (Color online) Band dispersion around W_1 along (a) the k_x, (b) k_y, and (c) k_z directions of TaAs, TaP, NbAs, and NbP. The k-space coordinate of each Weyl node is set to zero.

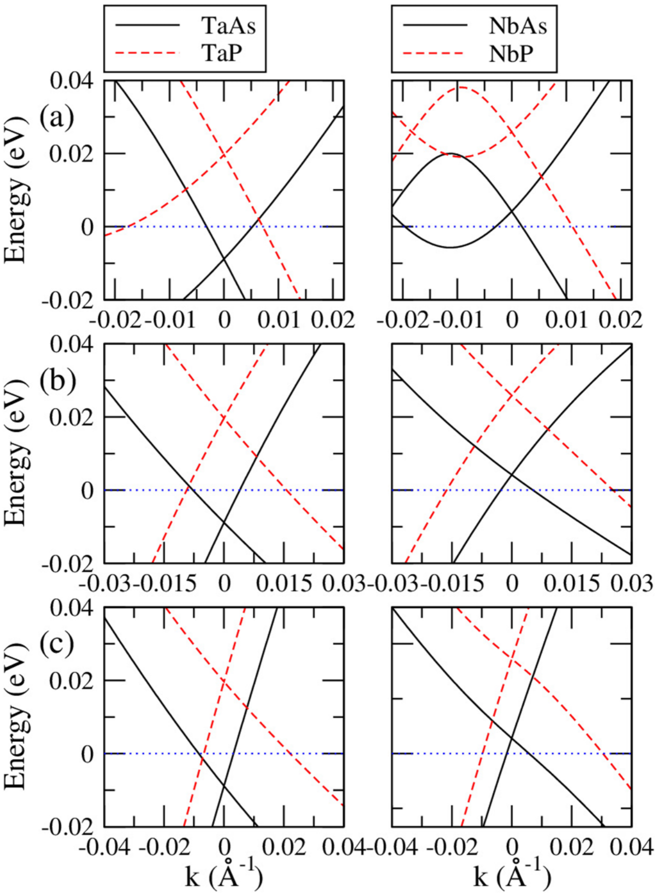

FIG. 9. (Color online) Band dispersion around W_2 along (a) the k_x, (b) k_y, and (c) k_z directions of TaAs, TaP, NbAs, and NbP. The k-space coordinate of each Weyl node is set to zero.

W_1 and W_2 along the k_x, k_y, and k_z directions are listed in Table III. As long as k is close enough to the Weyl nodes, the three-dimensional linear dispersive feature of Weyl cones is expected. It can be found that the velocities in Table III are highly anisotropic, and so are the band dispersions shown in Figs. 8 and 9. Consequently, the Fermi surface should exhibit such anisotropy. A detailed discussion of the Fermi surfaces will be addressed in the subsequent section.

TABLE III. Mean velocities at Weyl nodes along the x, y, and z directions in units of 10^5 m s^{-1}. Here, c and v are for the conduction band and the valence band, respectively.

	Velocity	Band	TaAs	TaP	NbAs	NbP
W_1	v_x	c	2.5	3.1	2.5	3.7
	v_x	v	−5.2	−5.7	−4.8	−5.7
	v_y	c	1.2	1.5	1.2	1.5
	v_y	v	−3.2	−3.6	−2.0	−3.0
	v_z	c	0.2	0.2	0.1	0.0(3)
	v_z	v	−0.2	−0.2	−0.1	−0.0(3)
W_2	v_x	c	2.4	2.3	2.4	2.1
	v_x	v	−4.3	−4.1	−3.3	−3.2
	v_y	c	3.5	3.0	2.3	2.1
	v_y	v	−1.7	−2.0	−1.2	−1.6
	v_z	c	4.3	4.4	3.7	3.8
	v_z	v	−1.6	−1.5	−1.1	−1.0

TABLE IV. Electron (e) and hole (h) carrier concentrations n, maximal areas A of cross sections on the yz, xz, and xy planes, and rms velocities $\bar{v}$ along the k_x, k_y, and k_z directions of Fermi surfaces (see Fig. 10). S_{W1} (S_{W2}) is the Fermi surface enclosing and evolved from the W_1 (W_2) Weyl node(s), and S_e (S_h) is an electron (hole) pocket Fermi surface not evolved from any Weyl node. The units for carrier concentration, area, and velocity are 10^{17} cm^{-3}, 10^{-3} Å^{-2}, and 10^5 m s^{-1}, respectively.

	Surface	n	A_{yz}	A_{xz}	A_{xy}	$\bar{v}_x$	$\bar{v}_y$	$\bar{v}_z$
TaAs	$S_{W1}(e)$	3.336	6.060	2.557	0.639	2.920	1.532	0.453
	$S_{W2}(e)$	0.134	0.244	0.237	0.226	2.055	1.579	1.763
	S_e	0.364	0.406	0.406	0.624	0.365	0.365	0.412
	S_h	2.201	7.332	0.310	1.639	4.051	0.670	1.372
TaP	$S_{W1}(e)$	48.98	23.67	15.87	4.687	3.270	1.594	0.767
	$S_{W2}(h)$	53.17	36.96	13.94	3.404	3.736	2.542	1.879
NbAs	$S_{W1}(e)$	14.60	15.97	6.882	1.752	3.750	1.370	0.542
	$S_{W2}(h)$	29.76	24.57	10.29	2.646	4.647	2.647	1.765
	S_e	0.196	1.704	0.375	0.060	2.331	1.131	0.194
	S_{h1}	1.925	3.533	2.299	0.470	2.815	1.922	0.600
	S_{h2}	0.155	1.410	0.037	0.104	3.692	0.695	1.887
NbP	$S_{W1}(e)$	32.64	31.47	10.78	2.805	4.047	1.653	0.932
	$S_{W2}(h)$	82.16	43.94	20.15	5.913	4.964	3.147	2.551
	S_{e1}	4.323	11.12	2.928	0.599	4.773	1.845	0.501
	S_{e2}	0.025	0.219	0.016	0.056	3.828	0.466	1.896
	S_{h1}	33.95	22.59	13.03	3.772	4.971	3.294	1.929

B. Fermi surface

The properties of Fermi surfaces discussed below were calculated using discrete grids in k space. The calculations were performed using a conventional unit cell. Each length of the grid was 0.0015, 0.0015, and 0.005 reciprocal lattice vector along the k_x, k_y, and k_z directions, respectively. Information regarding the volume and cross-sectional area of Fermi surfaces and the Fermi velocities for each compound are listed in Table IV.

1. TaAs

The Fermi surfaces of TaAs are formed by both electron and hole pockets, which are shown in Fig. 10. According to Table II, both W_1 and W_2 are below the Fermi energy, with the latter being closer to it. As a result, an electron pocket enclosing the W_1 or W_2 Weyl node is expected. The Fermi surface of W_1 is much bigger than that of W_2 and shows high anisotropy along k_z. Some distance away from the end of the Fermi surface of W_1, a hole pocket centered on the mirror plane appears and extends to the neighborhood of the Fermi surface of W_2. Since each of the S_{W1} and S_{W2} Fermi surfaces encloses one Weyl node, the Fermi surface is endowed with a ±1 Chern number [61]. Furthermore, the hole pocket does not surround any Weyl nodes, which is an outcome of the modulation of bands, and, consequently, carries a zero Chern number. The shape of the Fermi surfaces is reminiscent of the nodal rings in the absence of spin-orbit coupling. We note that different from the other

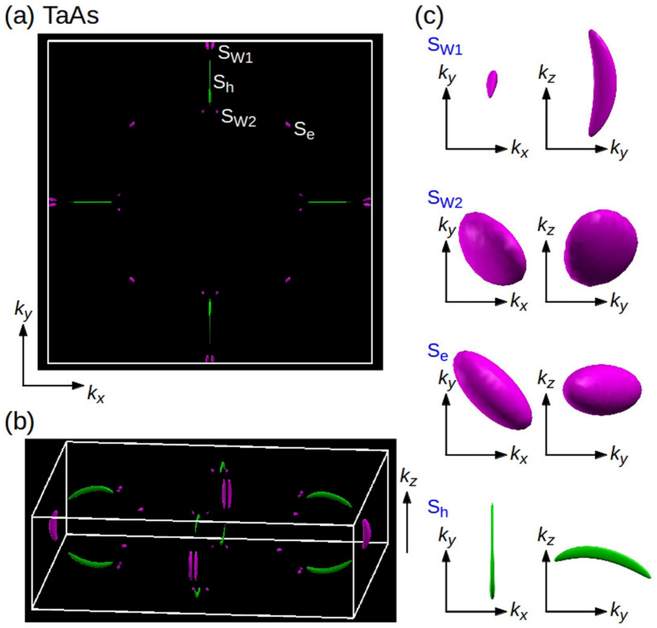

FIG. 10. (Color online) (a) Top view and (b) bird's-eye view of TaAs Fermi surfaces in the first Brillouin zone of a conventional unit cell with (c) more detailed plots. Electronlike and holelike Fermi surfaces are colored pink and green, respectively. S_{W1} (S_{W2}) is the Fermi surface enclosing the W_1 (W_2) Weyl node(s), and S_e (S_h) is an electron (hole) pocket that does not enclose any Weyl node.

compounds discussed below, the Fermi surfaces on two sides of a mirror plane are isolated instead of getting immersed, which is due to the distances between Weyl nodes and their energies relative to the Fermi energy. Furthermore, an electron pocket around (0.2425, 0.2425, 0) is found, which does not appear in other compounds. The details of the shapes and carrier concentrations can be found in Fig. 10 and Table IV. The maximal areas of the cross sections for the Fermi surfaces, which can be specifically measured by cyclotron experiments, are also listed in Table IV.

2. *TaP*

The Fermi surfaces of TaP are presented in Fig. 11. Contrary to TaAs, in which energies of both W_1 and W_2 are below the Fermi energy, the energies of W_1 and W_2 in TaP are below and above the Fermi energy, respectively, as shown in Table II. W_2 in TaP is enclosed by a hole pocket Fermi surface. Due to higher energies of Weyl nodes away from the Fermi energy, the volumes of Fermi surfaces are much larger (about 10–20 times for S_{W1}) than those in TaAs. Furthermore, a Fermi surface encloses more than one Weyl node. An electronlike Fermi surface encompasses a mirror pair of W_1 points, while a holelike Fermi surface covers two mirror pairs of W_2 points. Compared to that in TaAs, both electron and hole pockets take the shape of a crescent that is distributed more along the k_z direction. Except for these electron and hole pockets there is no other piece of Fermi surface. The carrier concentrations and maximal areas of cross sections are listed in Table IV.

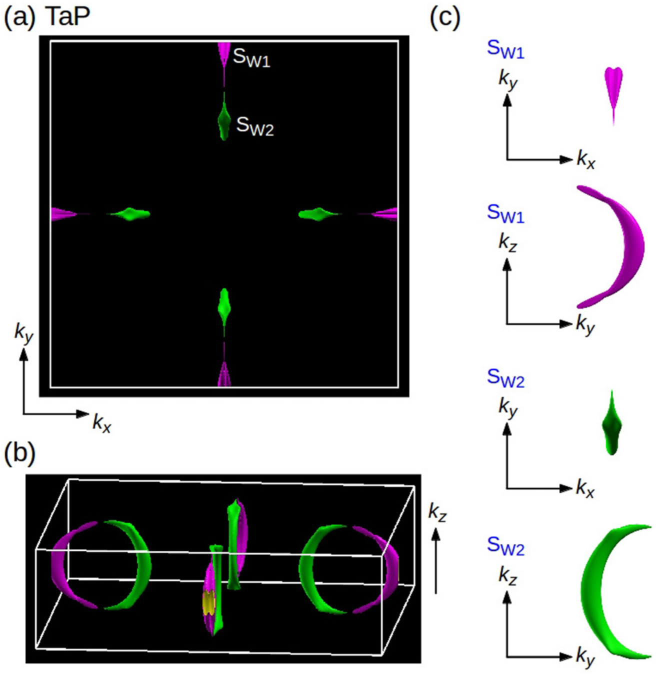

FIG. 11. (Color online) (a) Top view and (b) bird's-eye view of TaP Fermi surfaces in the first Brillouin zone of a conventional unit cell with (c) more detailed plots. Electronlike and holelike Fermi surfaces are colored pink and green, respectively. S_{W1} (S_{W2}) is the Fermi surface enclosing the W_1 (W_2) Weyl node(s).

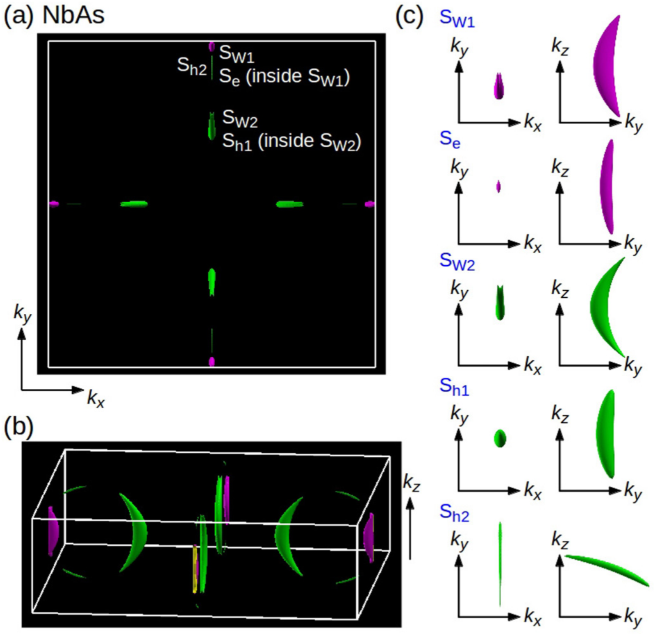

FIG. 12. (Color online) (a) Top view and (b) bird's-eye view of NbAs Fermi surfaces in the first Brillouin zone of a conventional unit cell with (c) more detailed plots. Electronlike and holelike Fermi surfaces are colored pink and green, respectively. S_{W1} (S_{W2}) is the Fermi surface enclosing and evolved from the W_1 (W_2) Weyl node(s), and S_e (S_h) is an electron (hole) pocket not evolved from the Weyl node.

3. NbAs

The Fermi surfaces of NbAs are presented in Fig. 12. In NbAs, the energy of W_1 and W_2 are below and above the Fermi energy, respectively. Three types of holelike Fermi surfaces are found in NbAs. The first kind encloses four W_2 points and passes through the $k_z = 0$ plane, like those found in TaP. The second kind is similar to those crescents elongated along the k_x or k_y direction in TaAs. The third kind cannot be seen in Fig. 12 because the Fermi energy cuts through two spin-split valence bands at $\vec{k} \approx (0,0.2152,0)$. Consequently, the inner surface is hidden inside the outer surface. In comparison with the W_1 points in TaAs and TaP, the two neighboring W_1 points are closer to each other. As a result, only one big crescent-shaped electron pocket containing two W_1 points is observed. Similar to the scenario of the two concentric-like hole pockets, there is also another electron pocket hidden inside the bigger Fermi surface near W_1. The carrier concentrations and maximal areas of cross sections for each Fermi surface are listed in Table IV.

4. NbP

The Fermi surfaces of NbP are presented in Fig. 13. Similar to TaP and NbAs, the energy of W_1 and W_2 in NbAs are below and above the Fermi energy, respectively. The two concentric-like hole Fermi surfaces split by spin-orbit coupling are also present in NbP as intersecting the $k_z = 0$ plane at $\vec{k} \approx (0,0.2042,0)$, giving rise to four crescent Fermi surfaces in the first Brillouin zone, with each surface containing one more surface inside. Each outer surface encloses one pair of W_2 points. In NbP, one long crescent electronlike Fermi surface resembling the shape of half a ring can be found. The surface becomes thinner while deviating from W_1, and the detailed shape is easier to observe in Fig. 13(c). There are two additional electronlike Fermi surfaces inside this long crescent surface, S_{e1} and S_{e2}. Referring to the band dispersion in Fig. 8, we have to carefully identify the concentric electron pockets. Although S_{e1} encloses one W_1 point, the associated band does not evolve from the band of Weyl nodes and therefore is a trivial Fermi surface. The size of surface S_{e2} is small and touches the limit for the chosen grid size. The carrier concentration and maximal areas of cross sections for each Fermi surface are listed in Table IV.

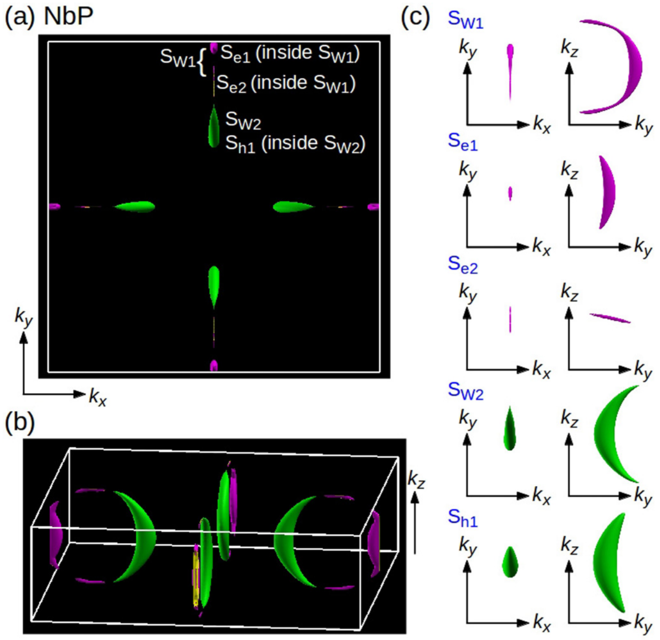

FIG. 13. (Color online) (a) Top view and (b) bird's-eye view of NbP Fermi surfaces in the first Brillouin zone of a conventional unit cell with (c) more detailed plots. Electronlike and holelike Fermi surfaces are colored pink and green, respectively. S_{W1} (S_{W2}) is the Fermi surface enclosing and evolved from the W_1 (W_2) Weyl node(s), and S_e (S_h) is an electron (hole) pocket not evolved from the Weyl node.

V. DISCUSSION

Several interesting properties of the charge carriers can be found even without the consideration of additional conditions, like applying magnetic or strain fields in first-principles calculations. We first note that the energy difference between W_1 and W_2 is ~10–100 meV, which is realistic to access by doping in real crystals. The Fermi energy for TaAs was experimentally found [38] to be located between W_1 and W_2 (E_{W1} and E_{W2}, respectively), which is approximately 11.5 meV above E_{W1} and therefore different from our calculations shown in Table II.

The energy difference between two Weyl nodes is directly related to the minimal area of the Fermi surface as a function of binding energy, with a larger separation, $|E_{W2} - E_{W1}|$, corresponding to a larger minimal Fermi surface. Referring to Table II, the energy differences of E_{W2} and E_{W1} are 0.0132, 0.0727, 0.0364, and 0.0793 eV for TaAs, TaP, NbAs, and NbP, respectively. Recall, $E_{W2} > E_{W1}$. Note that while the separation in momentum space of the Weyl nodes is determined by the strength of the spin-orbit coupling, the separation in energy of the Weyl nodes can be viewed as arising from the dispersion of the spinless line-node crossing, observed before spin-orbit coupling is introduced. Among the four Weyl semimetal compounds, the relatively small value for TaAs explains the relatively small carrier concentration, e.g., 0.134×10^{17} cm^{-3} for S_{W2}. Similarly, the largest hole pocket can be found in NbP, e.g., 82.16×10^{17} cm^{-3} for S_{W2}. The rich and tunable behavior of charge carriers in these four semimetals strongly suggests that these compounds are a good playground for engineering electronic properties through doping, strain, electric fields, magnetic fields, and/or other external perturbations.

Furthermore, we also point out that an abrupt change in the topology of the Fermi surface may occur by tuning the Fermi energy via, for example, doping, exhibiting a Lifshitz transition. Since each pair of Weyl nodes is located on two sides of the mirror plane, after turning on the spin-orbit coupling, the nodes are, in general, close to each other. Therefore, there exists a critical Fermi energy that can make the two Fermi surfaces, each enclosing the Weyl node(s) on one side of the plane, touch at one k point. By changing the critical Fermi energy, either one big surface enclosing both Weyl nodes or two small surfaces with each enclosing a single Weyl node can be formed. The Fermi surfaces of the W_1 or W_2 pairs in TaAs are an example of the latter case, while those in TaP, NbAs, and NbP are examples of the former case.

ACKNOWLEDGMENTS

Work at National University of Singapore is supported by the National Research Foundation, Prime Minister's Office, Singapore under its NRF fellowship (NRF Award No. NRF-NRFF2013-03). Research work at Princeton University is funded by US Department of Energy (DOE), Office of Science, Basic Energy Sciences Grant No. DE-FG-02-05ER46200. The work at Northeastern University was supported by the US DOE, Office of Science, Basic Energy Sciences Grant No. DE-FG-02-07ER46352, and benefited from Northeastern University's Advanced Scientific Computation Center (ASCC) and the NERSC supercomputing center through DOE Grant No. DE-AC02-05CH11231. S.M.H., G.C., and H.L.'s visits to Princeton University are funded by the Gordon and Betty Moore Foundations EPiQS Initiative through Grant GBMF4547 (Hasan).

C.-C.L. and S.-Y.X. contributed equally to this work.

---

[1] H. Weyl, Elektron und gravitation. I, Z. Phys. **56**, 330 (1929).

[2] C. Herring, Accidental degeneracy in the energy bands of crystals, Phys. Rev. **52**, 365 (1937).

[3] A. A. Abrikosov and S. D. Beneslavskii, Some properties of gapless semiconductors of the second kind, J. Low Temp. Phys. **5**, 141 (1971).

[4] H. B. Nielsen, M. Ninomiya, The Adler-Bell-Jackiw anomaly and Weyl fermions in a crystal, Phys. Lett. B **130**, 389 (1983).

[5] G. E. Volovik, *The Universe in a Helium Droplet* (Oxford University Press, Oxford, 2009).

[6] S. Murakami, Phase transition between the quantum spin Hall and insulator phases in 3D: Emergence of a topological gapless phase, New J. Phys. **9**, 356 (2007).

[7] X. Wan, A. M. Turner, A. Vishwanath, and S. Y. Savrasov, Topological semimetal and Fermi-arc surface states in the electronic structure of pyrochlore iridates, Phys. Rev. B **83**, 205101 (2011).

[8] K.-Y. Yang, Y.-M. Lu, and Y. Ran, Quantum Hall effects in a Weyl semimetal: Possible application in pyrochlore iridates, Phys. Rev. B **84**, 075129 (2011).

[9] L. Balents, Viewpoint: Weyl electrons kiss, Physics **4**, 36 (2011).

[10] A. A. Burkov and L. Balents, Weyl Semimetal in a Topological Insulator Multilayer, Phys. Rev. Lett. **107**, 127205 (2011).

[11] S.-M. Huang, S.-Y. Xu, I. Belopolski, C.-C. Lee, G. Chang, B. Wang, N. Alidoust, G. Bian, M. Neupane, C. Zhang, S. Jia, A. Bansil, H. Lin, and M. Z. Hasan, A Weyl Fermion semimetal with surface Fermi arcs in the transition metal monopnictide TaAs class, Nat. Commun. **6**, 7373 (2015).

[12] S.-Y. Xu *et al.*, Discovery of a Weyl fermion semimetal and topological Fermi arcs, Science **349**, 613 (2015).

[13] H. Weng, C. Fang, Z. Fang, B. A. Bernevig, and X. Dai, Weyl Semimetal Phase in Noncentrosymmetric Transition-Metal Monophosphides, Phys. Rev. X **5**, 011029 (2015).

[14] B. Q. Lv, H. M. Weng, B. B. Fu, X. P. Wang, H. Miao, J. Ma, P. Richard, X. C. Huang, L. X. Zhao, G. F. Chen, Z. Fang, X. Dai, T. Qian, and H. Ding, Experimental Discovery of Weyl Semimetal TaAs, Phys. Rev. X **5**, 031013 (2015).

[15] A. H. Castro Neto, F. Guinea, N. M. R. Peres, K. S. Novoselov, and A. K. Geim, The electronic properties of graphene, Rev. Mod. Phys. **81**, 109 (2009).

[16] S. Das Sarma, S. Adam, E. H. Hwang, and E. Rossi, Electronic transport in two-dimensional graphene, Rev. Mod. Phys. **83**, 407 (2011).

[17] M. Z. Hasan and C. L. Kane, Colloquium: Topological insulators, Rev. Mod. Phys. **82**, 3045 (2010).

[18] X.-L. Qi and S.-C. Zhang, Topological insulators and superconductors, Rev. Mod. Phys. **83**, 1057 (2011).

[19] F. D. M. Haldane, Attachment of surface "Fermi arcs" to the Bulk Fermi surface: "Fermi-level plumbing" in topological metals, arXiv:1401.0529.

[20] B. Singh, A. Sharma, H. Lin, M. Z. Hasan, R. Prasad, and A. Bansil, Topological electronic structure and Weyl semimetal in the TlBiSe$_2$ class of semiconductors, Phys. Rev. B **86**, 115208 (2012).

[21] A. M. Turner and A. Vishwanath, Beyond Band Insulators: Topology of Semi-metals and Interacting Phases, in *Topological Insulators: Fundamentals and Perspectives*, edited by F. Ortmann, S. Roche, and S. O. Valenzuela (John Wiley & Sons, New York, 2015).

[22] G. Xu, H. Weng, Z. Wang, X. Dai, and Z. Fang, Chern Semimetal and the Quantized Anomalous Hall Effect in HgCr$_2$Se$_4$, Phys. Rev. Lett. **107**, 186806 (2011).

[23] D. Bulmash, C.-X. Liu, and X.-L. Qi, Prediction of a Weyl semimetal in Hg$_{1-x-y}$Cd$_x$Mn$_y$Te, Phys. Rev. B **89**, 081106 (2014).

[24] J. Liu and D. Vanderbilt, Weyl semimetals from noncentrosymmetric topological insulators, Phys. Rev. B **90**, 155316 (2014).

[25] P. Hosur, S. A. Parameswaran, and A. Vishwanath, Charge Transport in Weyl Semimetals, Phys. Rev. Lett. **108**, 046602 (2012).

[26] H.-J. Kim, K.-S. Kim, J.-F. Wang, M. Sasaki, N. Satoh, A. Ohnishi, M. Kitaura, M. Yang, and L. Li, Dirac versus Weyl Fermions in Topological Insulators: Adler-Bell-Jackiw Anomaly in Transport Phenomena, Phys. Rev. Lett. **111**, 246603 (2013).

[27] S. A. Parameswaran, T. Grover, D. A. Abanin, D. A. Pesin, and A. Vishwanath, Probing the Chiral Anomaly with Nonlocal Transport in Three-Dimensional Topological Semimetals, Phys. Rev. X **4**, 031035 (2014).

[28] P. Hosur and X. Qi, Recent developments in transport phenomena in Weyl semimetals, C. R. Phys. **14**, 857 (2013).

[29] A. C. Potter, I. Kimchi, and A. Vishwanath, Quantum oscillations from surface Fermi arcs in Weyl and Dirac semimetals, Nat. Commun. **5**, 5161 (2014).

[30] Z. Fang, N. Nagaosa, K. S. Takahashi, A. Asamitsu, R. Mathieu, T. Ogasawara, H. Yamada, M. Kawasaki, Y. Tokura, and K. Terakura, The anomalous Hall effect and magnetic monopoles in momentum space, Science **302**, 92 (2003).

[31] G. B. Halász and L. Balents, Time-reversal invariant realization of the Weyl semimetal phase, Phys. Rev. B **85**, 035103 (2012).

[32] A. A. Zyuzin, S. Wu, and A. A. Burkov, Weyl semimetal with broken time reversal and inversion symmetries, Phys. Rev. B **85**, 165110 (2012).

[33] T. Das, Weyl semimetal and superconductor designed in an orbital-selective superlattice, Phys. Rev. B **88**, 035444 (2013).

[34] T. Ojanen, Helical Fermi arcs and surface states in time-reversal invariant Weyl semimetals, Phys. Rev. B **87**, 245112 (2013).

[35] M. V Berry, Quantal phase factors accompanying adiabatic changes, Proc. R. Soc. London, Ser. A **392**, 45 (1984).

[36] C. Zhang, Z. Yuan, S. Xu, Z. Lin, B. Tong, M. Z. Hasan, J. Wang, C. Zhang, and S. Jia, Tantalum Monoarsenide: An Exotic Compensated Semimetal, arXiv:1502.00251.

[37] X. Huang, L. Zhao, Y. Long, P. Wang, D. Chen, Z. Yang, H. Liang, M. Xue, H. Weng, Z. Fang, X. Dai, and G. Chen, Observation of the Chiral-Anomaly-Induced Negative Magnetoresistance in 3D Weyl Semimetal TaAs, Phys. Rev. X **5**, 031023 (2015).

[38] C. Zhang, S.-Y. Xu, I. Belopolski, Z. Yuan, Z. Lin, B. Tong, N. Alidoust, C.-C. Lee, S.-M. Huang, H. Lin, M. Neupane, D. S. Sanchez, H. Zheng, G. Bian, J. Wang, C. Zhang, T. Neupert, M. Z. Hasan, and S. Jia, Observation of the Adler-Bell-Jackiw chiral anomaly in a Weyl semimetal, arXiv:1503.02630.

[39] S.-Y. Xu *et al.*, Discovery of a Weyl fermion state with Fermi arcs in niobium arsenide, Nat. Phys. **11**, 748 (2015).

[40] S.-Y. Xu *et al.*, Experimental discovery of a topological Weyl semimetal state in TaP, arXiv:1508.03102.

[41] B. Q. Lv, N. Xu, H. M. Weng, J. Z. Ma, P. Richard, X. C. Huang, L. X. Zhao, G. F. Chen, C. E. Matt, F. Bisti, V. N. Strokov, J. Mesot, Z. Fang, X. Dai, T. Qian, M. Shi, and H. Ding, Observation of Weyl nodes in TaAs, Nat. Phys. **11**, 724 (2015).

[42] N. Xu *et al.*, Observation of Weyl nodes and Fermi arcs in TaP, arXiv:1507.03983.

[43] L. X. Yang, Z. K. Liu, Y. Sun, H. Peng, H. F. Yang, T. Zhang, B. Zhou, Y. Zhang, Y. F. Guo, M. Rahn, D. Prabhakaran, Z. Hussain, S.-K. Mo, C. Felser, B. Yan, and Y. L. Chen, Weyl semimetal phase in the non-centrosymmetric compound TaAs, Nat. Phys. **11**, 728 (2015).

[44] N. J. Ghimire, Y. Luo, M. Neupane, D. J. Williams, E. D. Bauer, and F. Ronning, Magnetotransport of single crystalline NbAs, J. Phys. Condens. Matter **27**, 152201 (2015).

[45] C. Shekhar, A. K. Nayak, Y. Sun, M. Schmidt, M. Nicklas, I. Leermakers, U. Zeitler, Y. Skourski, J. Wosnitza, Z. Liu, Y. Chen, W. Schnelle, H. Borrmann, Y. Grin, C. Felser, and B. Yan, Extremely large magnetoresistance and ultrahigh mobility in the topological Weyl semimetal candidate NbP, Nat. Phys. **11**, 645 (2015).

[46] Y. Luo, N. J. Ghimire, M. Wartenbe, H. Choi, M. Neupane, R. D. McDonald, E. D. Bauer, J. Zhu, J. D. Thompson, and F. Ronning, A novel electron-hole compensation effect in NbAs, arXiv:1506.01751.

[47] Z. Wang, Y. Zheng, Z. Shen, Y. Zhou, X. Yang, Y. Li, C. Feng, and Z.-A. Xu, Helicity protected ultrahigh mobility Weyl fermions in NbP, arXiv:1506.00924.

[48] C. Shekhar, F. Arnold, S.-C. Wu, Y. Sun, M. Schmidt, N. Kumar, A. G. Grushin, J. H. Bardarson, R. Donizeth dos Reis, M. Naumann, M. Baenitz, H. Borrmann, M. Nicklas, E. Hassinger, C. Felser, and B. Yan, Large and unsaturated negative magnetoresistance induced by the chiral anomaly in the Weyl semimetal TaP, arXiv:1506.06577.

[49] P. J. W. Moll, A. C. Potter, B. Ramshaw, K. Modic, S. Riggs, B. Zeng, N. J. Ghimire, E. D. Bauer, R. Kealhofer, N. Nair, F. Ronning, and J. G. Analytis, Magnetic torque anomaly in the quantum limit of the Weyl semi-metal NbAs, arXiv:1507.06981.

[50] C. Zhang, C. Guo, H. Lu, X. Zhang, Z. Yuan, Z. Lin, J. Wang, and S. Jia, Large magnetoresistance over an extended temperature regime in monophosphides of tantalum and niobium, Phys. Rev. B **92**, 041203(R) (2015).

[51] C. Zhang, Z. Lin, C. Guo, S.-Y. Xu, C.-C. Lee, H. Lu, S.-M. Huang, G. Chang, C.-H. Hsu, H. Lin, L. Li, C. Zhang, T. Neupert, M. Zahid Hasan, J. Wang, and S. Jia, Quantum phase transitions in weyl semimetal tantalum monophosphide, arXiv:1507.06301.

[52] J. Du, H. Wang, Q. Mao, R. Khan, B. Xu, Y. Zhou, Y. Zhang, J. Yang, B. Chen, C. Feng, and M. Fang, Unsaturated both large positive and negative magnetoresistance in Weyl semimetal TaP, arXiv:1507.05246.

[53] I. Morrison, D. M. Bylander, and L. Kleinman, Nonlocal Hermitian norm-conserving Vanderbilt pseudopotential, Phys. Rev. B **47**, 6728 (1993).

[54] T. Ozaki, Variationally optimized atomic orbitals for large-scale electronic structures, Phys. Rev. B **67**, 155108 (2003).

[55] T. Ozaki *et al.*, OPENMX, http://www.openmx-square.org/.

[56] G. Theurich and N. A. Hill, Self-consistent treatment of spin-orbit coupling in solids using relativistic fully separable ab initio pseudopotentials, Phys. Rev. B **64**, 073106 (2001).

[57] W. Kohn and L. J. Sham, Self-consistent equations including exchange and correlation effects, Phys. Rev. **140**, A1133 (1965).

[58] J. P. Perdew, K. Burke, and M. Ernzerhof, Generalized Gradient Approximation Made Simple, Phys. Rev. Lett. **77**, 3865 (1996).

[59] J.-H. Zhou, H. Jiang, Q. Niu, and J.-R. Shi, Topological invariants of metals and the related physical effects, Chin. Phys. Lett. **30**, 027101 (2013).

[60] C.-K. Chiu and A. P. Schnyder, Classification of reflection-symmetry-protected topological semimetals and nodal superconductors, Phys. Rev. B **90**, 205136 (2014).

[61] D. Gosálbez-Martínez, I. Souza, and D. Vanderbilt, Chiral degeneracies and Fermi-surface Chern numbers in bcc Fe, Phys. Rev. B **92**, 085138 (2015).